Journal of
Materials Chemistry A

Materials for energy and sustainability

Accepted Manuscript

This article can be cited before page numbers have been issued, to do this please use: J. Liu, H. Cao, Y. Zhang, J. Ding and Y. Wang, *J. Mater. Chem. A*, 2025, DOI: 10.1039/D5TA03824C.

ROYAL SOCIETY OF CHEMISTRY

rsc.li/materials-a

View Article Online
DOI: 10.1039/D5TA03824C

Quasi-Solid-state Li-ion Hybrid Capacitor Based on a Colloidal Metal-Organic Framework Interwoven by In-situ Polymerized PANI

Jiale, Liu,[a] Hui Cao,[a] Yidong Zhang,*[a] Jianfei Ding,*[a] Yuan Wang,*[b]

a School of Chemistry and Chemical Engineering, Yancheng Institute of Technology, Yancheng, 224051, PR China

b School of Chemistry and Environmental Engineering, Yancheng Teachers University, Yancheng, 224002, PR China

*Corresponding authors:

* Yidong Zhang **E-mail**: zhangyidong@ycit.edu.cn

* Yuan Wang **E-mail**: wangy03@yctu.edu.cn

View Article Online
DOI: 10.1039/D5TA03824C

Abstract

Metal-organic frameworks (MOFs) have emerged as promising candidates for advanced energy storage systems. However, their practical application is hindered by intrinsic conductivity limitations. This study introduces a novel in-situ gel-confined polymerization strategy to fabricate MOFs gel/polyaniline (MOG/PANI) composites with precisely tunable architectures. Systematic adjustment of PANI content elucidates critical composition-property relationships, where the optimized MOG/PANI-3 composite exhibits uniform component distribution and enhanced interfacial interactions. The developed electrode exhibits an impressive specific capacitance of 423.8 F g^{-1} at a current density of 1 A g^{-1}. Electrochemical studies showed that excessive incorporation of PANI induces detrimental aggregation phenomena that degrade impedance characteristics. The study developed a quasi-solid-state Li-ion hybrid capacitor using MOG/PANI-3 cathode paired with activated carbon anode. This configuration achieves an exceptional energy density of 41.3 W h kg^{-1} at 900 W kg^{-1}. Furthermore, it maintains 87.3% capacitance retention after 4000 cycles at 5 A g^{-1}, demonstrating acceptable cycling stability. This gel-confined synthesis method effectively addresses the poor conductivity issues inherent in MOFs-based electrode materials. Simultaneously, it creates a flexible platform for developing multifunctional hybrid materials tailored to next-generation energy storage systems.

Keywords: MOG; PANI; Supercapacitor; In-situ polymerization; Li-ion capacitor

View Article Online
DOI: 10.1039/D5TA03824C

1. Introduction

Supercapacitors, which are advanced energy storage systems with high power density, serve as important components in energy conversion architectures requiring rapid response capabilities[1, 2]. These devices are characterized by accelerated charge-discharge kinetics and remarkable cycling stability, making them attractive candidates for mitigating contemporary energy challenges[3-5]. Nevertheless, their practical implementation faces constraints due to comparatively lower energy storage capacities relative to conventional battery systems. The electrochemical performances of supercapacitors are primarily determined by the architecture of their electrode materials[6]. Therefore, it is essential to strategically develop cost-effective and high-performance electrode materials to facilitate innovations in next-generation energy storage systems[7, 8]. As an emerging class of porous crystalline materials, metal-organic frameworks (MOFs) are formed through the coordination bonds between metal-containing nodes and multifunctional organic linkers. Their distinctive structure enables excellent material properties, including ultrahigh surface areas, hierarchically tunable porosity, and designable molecular architectures[9, 10]. These features enable MOFs to theoretically achieve a substantial electric double-layer capacitance (EDLC), facilitating efficient ion adsorption and charge storage[11, 12]. Consequently, MOFs are considered promising candidates for the advancement of high-performance supercapacitors. Despite their significant potential, MOFs face certain challenges when used alone. Their application in electrochemical energy storage is limited by insufficient conductivity, which hinder their ability to fully meet the requirements of

View Article Online
DOI: 10.1039/D5TA03824C

modern energy storage technologies.

A highly effective strategy to enhance the conductivity of MOF-based supercapacitors involves systematically designing their structures by fully exploiting the unique advantages of MOFs, such as exceptional porosity, in conjunction with conductive polymers renowned for their superior conductivity[13, 14]. Among various conductive polymers, polyaniline (PANI) exhibits pseudocapacitive properties through rapid and reversible redox reactions, enabling additional charge storage via faradaic mechanisms[15, 16]. The integration of EDLC from MOFs and the pseudocapacitance of PANI significantly boosts overall capacitance and energy density, thereby enhancing specific capacitance[17]. For example, Wang et al. first integrated MOF materials (specifically ZIF-67) with PANI via electrochemical deposition to create a novel hybrid supercapacitor electrode. In this architecture, PANI chains serve as electron transport bridges interconnecting the MOF crystals and the external circuit, significantly enhancing overall conductivity and enabling high-performance flexible quasi-solid-state devices through synergistic effect[18]. Moreover, incorporating PANI into MOFs can make the ultrahigh surface area of MOFs electrochemically accessible, leading to superior charge transfer performance in the electrode material[19, 20]. However, achieving this goal is challenging due to the limitations of the solid-solid interface in the traditional construction strategy for composite materials. The primary difficulties can be summarized as follows: (i) The conventional physical mixing techniques, such as solution-phase blending, ultrasonication, and ball-milling processes, generally result in MOFs/PANI

View Article Online
DOI: 10.1039/D5TA03824C

composites with inadequate interfacial bonding strength owing to limited chemical interactions. These ex-situ synthesis methods typically produce composite architectures where the interfaces are predominantly governed by Van der Waals forces. This results in inefficient charge/mass transfer and insufficient electron transfer pathways during electrode operation. (ii) In the case of the in-situ incorporation strategy, the absence of specific anchoring sites on MOFs complicates the selective coating of MOFs crystal particles with PANI, often leading to the filling of other spaces instead. Consequently, the resulting composites exhibit poor uniformity. For example, Saha et al. PANI nanofibers onto the surface and between the layers of V-PMOF via an in-situ oxidative polymerization process. However, due to the lack of effective anchoring sites on the surface of MOF nanosheets, interaction between V-PMOF and PANI relied solely on electrostatic attraction. This hindered effective integration, resulting in poor dispersion of the composite material. Consequently, the V-PMOF@PANI composite achieved only a maximum specific capacitance of 322 F g^{-1} (at 0.5 A g^{-1})[21]. Therefore, taking these factors into consideration, it is highly imperative to develop a novel synthesis strategy to ensure that the fabricated MOFs/PANI composites possess both superior interfacial contact properties and uniformity.

In this study, we developed a novel gel-confined synthesis strategy to incorporate PANI within colloidal MOFs (as illustrated in Figure 1). Specifically, we chose MIL-100-Cr as the gel matrix (denoted as MOG). MIL-100-Cr is composed of benzene tricarboxylic acid ligands coordinated with chromium clusters, exhibiting remarkable

View Article Online
DOI: 10.1039/D5TA03824C

stability in aqueous, acidic, and thermal environments[22]. More importantly, MIL-100-Cr can undergo a gelation transition through a simple hydrothermal process without requiring hydrofluoric acid (HF). This colloidal state of MOFs serves as an intermediate phase between solid and liquid, effectively overcoming the challenge of poor interfacial contact inherent in traditional solid-state synthesis methods. Due to the uniform infiltration of the liquid solvent into the colloidal MOFs matrix, aniline solution can be rapidly and homogeneously dispersed throughout the macroscopically continuous MOFs phase via liquid-phase diffusion. Subsequently, PANI is generated via in situ polymerization within the confined spaces of the gel matrix, ensuring the uniform distribution of the resulting polyaniline. Moreover, the resulting MOFs/PANI xerogel exhibits a tightly packed, uniform, and dense structure, leveraging the synergistic benefits of gel-like MOFs and PANI networks. This architecture outperforms those achieved through conventional ex-situ physical blending techniques. To assess its potential for use in supercapacitor, different quantities of PANI were added to explore the impact of PANI content on the structural characteristics and electrochemical lithium storage capabilities of MOG/PANI composites. It was determined that a PANI proportion of 10% yields an optimal configuration for the MOG/PANI architecture. This enhances the rapid charge transfer property of electrolyte ions at the electrode and boosts the supercapacitor performance. Additionally, a quasi-solid-state Li-ion hybrid capacitor (QSLHC) device was constructed, showcasing favorable practical application prospects. Our research presents a novel methodology for constructing MOFs/polymer hybrids

View Article Online
DOI: 10.1039/D5TA03824C

through advanced interface engineering strategies, specifically tailored for high-performance lithium-ion capacitors that demand concurrent enhancements in both energy density and power density performances.

2. Experimental section

2.1 Synthesis of MOG/PANI composites

All chemicals and solvents were of commercial analytical quality and were utilized as received, without undergoing any additional purification processes. First, the MIL-100-Cr gel (MOG) was synthesized according to previously reported methods with minor modifications[23]. Under standardized synthesis conditions, chromium(III) nitrate nonahydrate (15 mmol) and 1,3,5-benzenetricarboxylic acid (H_3BTC, 10 mmol) were separately dissolved in anhydrous ethanol (30 mL) with the aid of magnetic stirring. Subsequently, the two solutions were rapidly combined and sonicated for 30 minutes to ensure complete mixing. Following thorough mixing, the solution was transferred into a Teflon-coated stainless steel autoclave and subjected to a hydrothermal treatment at 120 °C for two hours. Subsequently, the resulting gel was aged at room temperature for 24 hours. Next, the wet gel underwent three cycles of solvent exchange (12 hours) with ethanol. The purpose of this step is to clean the as-synthesized gel to remove the residual trace amounts of reactants that were not fully reacted during the synthesis process. It was further subjected to a 12-hour solvent exchange process by immersion in an aniline-ethanol solution. Thereafter, the gel (0.1 g ml^{-1}) was immersed in 60 ml $(NH)_4S_2O_8$ solution to induce in-situ polymerization. The molar ratio of aniline to ammonium persulfate was maintained at 1:1.2. After

View Article Online
DOI: 10.1039/D5TA03824C

reacting for 12 hours at refrigerated conditions (0 °C), the composite gel was dried at 80 °C in an oven to obtain a xerogel. The synthesized hybrid xerogel composites were assigned the designation MOG/PANI-x (x = 0-5), corresponding to the use of aniline solutions containing varying weight ratios (0%, 1%, 5%, 10%, 15%, and 20%) relative to the MOG matrix during the fabrication process. The numerical suffix systematically indicates the incremental increase in polyaniline precursor concentration employed in the composite synthesis.

2.2 Characterizations

Material characterization was systematically performed through multiple analytical techniques. Crystalline phase identification was achieved by X-ray diffraction (XRD) analysis employing a Bruker D8 Advance diffractometer with Cu Kα radiation. Molecular vibration patterns were investigated using Fourier-transform infrared spectroscopy (FTIR) collected on a Nicolet iS10 spectrometer, with spectral acquisition covering the 500-4000 cm^{-1} range. Surface topography examination was carried out using a Hitachi Regulus-8100 field-emission scanning electron microscope (SEM) operated under high-vacuum conditions. Chemical state analysis was complemented by X-ray photoelectron spectroscopy (XPS) measurements performed on a Shimadzu/Kratos AXIS Ultra DLD X-ray photoelectron spectrometer. Transmission electron microscopy (TEM) was carried out on Tecnai G2 F30. The N_2 adsorption-desorption isotherms were measured using Quantachrome AutosorbiQ-C at 77 K. Electrical conductivity measurements were carried out at 300 K in ambient atmosphere by Four-Point Probe Electronic Technology (RTS-8).

View Article Online
DOI: 10.1039/D5TA03824C

2.3 Electrochemical measurements

The electrode fabrication process involved homogenously combining active material particles with conductive Super P carbon additive and PTFE polymeric binder in a precisely controlled 8:1:1 mass ratio through mechanical mixing. The resultant viscous slurry was uniformly coated onto current collector (Ni Foam) substrates followed by a vacuum oven dehydration protocol at 80 °C for 24 hours to ensure complete solvent removal. Precise mass loading control achieved active material deposition quantities of 2.0 ± 0.1 mg per electrode. Electrochemical characterization was conducted using a CHI 660E potentiostat system (Chenhua Instruments, Shanghai) employing a three-electrode cell architecture with 1 M lithium sulfate aqueous electrolyte. The electrochemical cell configuration comprised a platinum mesh auxiliary electrode and saturated calomel reference electrode (SCE) calibrated against standard redox potentials. A customized electrolytic cell was employed to ensure a fixed distance (>1 cm) between the working electrode, counter electrode, and reference electrode, preventing short circuits and measurement errors during three-electrode testing. Frequency-dependent impedance characteristics were quantified using electrochemical impedance spectroscopy (EIS), with sinusoidal perturbations applied from 100 kHz down to 0.1 Hz. The specific capacitances (C_{sp}, F g^{-1}) were calculated from galvanostatic charge-discharge (GCD) tests using the following formula[24]:

$$C_{sp} = I \times \Delta t / (m \times \Delta V) \quad (1)$$

The symbols are defined as follows: electrode current I (A), discharge time Δt,

View Article Online
DOI: 10.1039/D5TA03824C

(s), active material mass m (g), and potential window ΔV (V).

2.4 Fabrication process of the two-electrode device

The quasi-solid-state energy storage device was constructed using a MOG/PANI-x composite as the cathode and commercially activated carbon (AC) as the anode. A polyvinyl alcohol-based electrolyte system (PVA-Li_2SO4, 1 M concentration) served as the ionic conductive medium. During the preparation of the electrolyte, 2.00 g of PVA powder was first dissolved in 20 mL of deionized water (Milli-Q grade) to form a homogeneous solution. This solution was then thermally processed at 90 °C for 120 minutes. After ensuring complete dissolution, the resulting viscous polymer solution was transferred to the ambient environment. After cooling, the PVA aqueous solution was dropped into the mold and concentrated to prepare solid gel films. Subsequently, the cut gel membrane pieces were repeatedly immersed and exchanged in a 1 M Li_2SO_4 solution for 12 hours. The obtained PVA-Li_2SO_4 gel film was then sandwiched between nickel foam electrodes coated with cathode and anode materials to form a sandwich structure. Following this, the quasi-solid-state device was obtained by introducing the electrode tabs and a plastic encapsulation shell. The mass ratio between the cathode and anode materials was calculated due to equation (2)[25]:

$$m^+ / m^- = (C^- \times \Delta V^-) / (C^+ \times \Delta V^+) \qquad (2)$$

In this configuration, the cathode and anode materials exhibit distinct specific capacitance values (denoted as C^+ and C^- respectively). The mass ratio between the cathodic (m^+) and anodic (m^-) active materials was optimized to 0.65 through

View Article Online
DOI: 10.1039/D5TA03824C

systematic calculation. The mass loading of the positive electrode was set to ~6.50 mg.

3 Results and discussion

3.1 Characterization of MOG/PANI-x

The MIL-100-Cr based MOG was synthesized by simply mixing a metal salt solution with a carboxylic acid solution under hydrothermal conditions. The formation of MOG is driven by coordination interactions, which can be influenced by crystallization or precipitation processes[26]. Typically, the gelation mechanism consists of three stages: the initial coordination between metal ions and ligands to form MOFs chains, the subsequent aggregation of these chains into MOFs particles, and finally the assembly of MOFs particles into hierarchical MOG structures[27]. In the early stages, Cr ions coordinate with BTC to generate small MOFs clusters that continue to grow until all Cr ions are fully coordinated. However, the rapid reduction of Cr centers disrupts the growth of crystallographic chains, resulting in non-crystallographic supramolecular gels. Within these gel networks, the solvent molecules are uniformly encapsulated around solid MOFs supramolecules, creating a liquid phase that serves as a macroscopically uniform and continuous confinement environment for the in-situ polymerization of aniline. This process enhances the uniform dispersion of MOFs and polyaniline molecules under conditions of strong interfacial interactions. To further investigate the structural changes in MOG/PANI hybrids as a function of PANI content, XRD analyses were conducted on MOG/PANI-x samples, with results presented in Figure 2a. Comparative analysis

View Article Online
DOI: 10.1039/D5TA03824C

indicates that the characteristic peak positions in these patterns are in excellent agreement with the reference data that simulated from MIL-100-Cr (CCDC 648835). This structural congruence confirms the successful incorporation of MOFs components into the hybrid matrix[28]. It is worth noting that all patterns display broadened peaks, which reflect reduced crystallinity of MOG, aligning with established mechanisms in gelatinous MOF systems documented in previous studies: i) Physically constrained polymerization processes inducing MOFs cluster formation, and ii) Nanoscale hetero-aggregation of MOFs building blocks during sol-gel transition[29]. The X-ray diffraction pattern displays prominent diffraction peaks at 20.6° and 25.7°, which can be ascribed to the (100) and (110) crystallographic planes of PANI, respectively. This confirms the successful incorporation of PANI into the MOG matrix [30]. Importantly, increasing PANI loading results in detectable peak shifts ($\Delta\theta \approx 0.1\text{-}0.3°$), suggesting that PANI intercalation influences the supramolecular organization of the composite via secondary bonding interactions, particularly π-conjugated interactions between aromatic groups. Figure 2b presents the FTIR spectra of MOG/PANI-x composites, illustrating the chemical bonding and interactions within different samples. Infrared spectral analysis of MOG reveals distinct vibrational signatures within the range of 1403 to 1707 cm^{-1}, which can be chemically attributed to the stretching vibrations of carboxyl groups. Peaks ranging from 700 to 600 cm^{-1} are associated with the Cr-O bond in Cr3 nodes[31]. The aromatic ring's C-H and C-C bonds can be identified at approximately 1715 and 1446 cm^{-1}, respectively. The C-C and C-H stretching vibrations of the benzenoid rings

View Article Online
DOI: 10.1039/D5TA03824C

occur around 1586 and 1447 cm^{-1}. The IR spectra of the MOG/PANI-x composites also exhibit characteristic bands of PANI, with a minor shift observed. The peak near 1550 cm^{-1} is linked to the C=N skeletal vibration within the quinoid ring. The characteristic ν(C-N) stretching mode exhibits a pronounced absorption band centered at 1304 cm^{-1} in the vibrational spectrum. Additionally, the peak at 1130 cm^{-1} corresponds to the $C\text{-}N^{+}$ vibration mode, indicating the incorporation of doped PANI[32]. The spectra of MOG and PANI show characteristic bands that align with those documented in the literature, confirming the successful synthesis of MOG/PANI-x composites as all key bands for MOG and PANI are clearly visible.

The surface morphology and hierarchical architecture of MOG/PANI-x were systematically evaluated through scanning electron microscopy at different magnifications. As depicted in Figure 3, each sample exhibits a tightly packed and dense architecture composed of nano particles, with PANI incorporated into the MOG matrix. In composites containing low levels of PANI, such as MOG/PANI-1 and MOG/PANI-2, the presence of PANI is scarcely detectable. As the PANI content increases, isolated PANI regions become visible, indicating excellent compatibility. PANI remains uniformly distributed within the MOG host without compromising its compact structure. This homogeneous distribution was further confirmed by EDS analysis (Figure S1), which detected the chemical elements Cr, C, N, and O and demonstrated their uniform dispersion throughout the material, highlighting the favorable structure of MOG/PANI-3. Additionally, it was observed that the distribution of N elements is relatively sparse, resembling the even scattering of stars

View Article Online
DOI: 10.1039/D5TA03824C

across the night sky. This indicates that PANI is evenly integrated within MOG without obvious aggregating. However, when the PANI content rises to 15% and 20%, as seen in MOG/PANI-4 and MOG/PANI-5, excess PANI tends to separate from the MOG matrix, leading to agglomeration and non-uniform dispersion of PANI. Based on the morphological findings, MOG/PANI-3 demonstrates the highest potential for constructing advanced MOG/PANI structures suitable for electrochemical applications. Therefore, we further conducted morphological analysis on MOG/PANI-3 through TEM characterization. As shown in Figure S2a and 2b, PANI exhibits a nanofiber morphology (as indicated by the white arrows in the figure), and can be uniformly dispersed within the MOF gel matrix. This is corroborated from the results obtained from the previous SEM characterization. These findings collectively confirm that the solid-liquid spatial confinement structure within the MOF gel matrix can facilitate the rapid feeding of aniline and provide sufficient space for the growth of PANI, which is crucial for the formation of PANI fiber-like long chains.

Furthermore, to investigate the influence of PANI content on the pore structure of MOG, we conducted N_2 adsorption-desorption isotherm measurements on the series MOG/PANI-x composites. As illustrated in Figure S3a, all isotherms exhibited characteristics of Type I. The specific surface area (SSA) of MOG/PANI-1, which contained the lowest PANI content, was measured to be 429.4 $m^2 g^{-1}$, a value closely aligned with previously reported data for colloidal MOF materials[23]. With the gradual increase in PANI content, the SSA of the resulting composites decreased

View Article Online
DOI: 10.1039/D5TA03824C

progressively. The SSA of MOG/PANI-2, MOG/PANI-3, MOG/PANI-4 and MOG/PANI-5 are 393.7, 345.3, 262.9 and 221.0 $m^2 g^{-1}$, respectively. This trend can be attributed to the relatively low SSA of PANI compared to that of the MOF matrix, effectively diluting the overall surface area of the composite. Moreover, the incorporation of PANI may partially block the pores of the MOF surface as well as the interparticle pores inherent in the colloidal structure. Pore size distribution analysis based on the BJH method (Figure S3b) revealed that, at lower PANI loadings, the composite retained the original mesoporous range of the MOF matrix (2-4 nm). However, when the PANI content exceeded 15% (MOG/PANI-4 and MOG/PANI-5), the pore size distribution shifted gradually toward 2 nm. The reduction in mesopore volume suggests that excessive PANI loading may lead to the infiltration of PANI chains into the MOF pores. Considering both the dispersion uniformity and pore structure characteristics, the analytical results indicate that MOG/PANI-3 possesses superior potential for electrochemical energy storage.

XPS analysis was strategically employed to characterize the elemental composition and oxidation states of MOG/PANI-3, motivated by its superior structural properties. The corresponding wide-scan XPS spectrum is displayed in Figure S4. The sample's Cr 2p, O 1s, N 1s, and C 1s components account for 3.26%, 26.59%, 1.26%, and 68.89% atomic percentages, respectively. As shown in Figure 4a, the Cr 2p core-level spectra consist of two peaks at $2p_{3/2}$ (578.3 eV) and $2p_{1/2}$ (587.7 eV), which are indicative of Cr^{3+} ions and confirm the successful synthesis of Cr-MOG[33]. The deconvoluted C 1s spectrum (Figure 4b) showed three predominant

View Article Online
DOI: 10.1039/D5TA03824C

contributions: the lowest binding energy peak at 284.8 eV was attributed to sp²-hybridized carbon structures, followed by intermediate (286.4 eV) and high-energy (288.7 eV) components assigned to oxygen-containing functionalities (C-O-C and C=O bonds, respectively)[34]. The deconvolution analysis of the N 1s XPS spectrum for MOG/PANI-3 (Figure 4c) reveals three chemically distinct nitrogen species. The primary component observed at 399.8 eV demonstrates characteristic binding energy of imine-type nitrogen (-NH=). A secondary peak centered at 400.9 eV matches the electronic environment of amine linkages (-NH-), while the highest energy component positioned at 402.1 eV indicates the presence of nitrogen atoms in a cationic state, corresponding to protonated amine species (-N^+-)[35]. The quantitative analysis of the deconvoluted N 1s spectra indicates that the N^+/N ratio in the polyaniline component of the MOG/PANI-3 composite significantly surpasses the threshold of 0.1. In polyaniline systems, the relative abundance of protonated imine (N^+) to deprotonated amine (N) units is a critical parameter reflecting the polymer's proton doping level. This finding conclusively demonstrates that the in-situ space confined synthesis strategy achieves optimal doping efficiency in PANI, which is intrinsically linked to its enhanced charge transport capabilities. The resultant superior electrical conductivity, achieved through this structural optimization, enables the formation of continuous charge transport networks within the MOG/PANI composite structure, wherein the PANI components function as molecular bridges connecting adjacent MOFs subunits. Furthermore, the oxygen speciation analysis identified two predominant chemical states through peak fitting: (i) oxygen atoms in carboxyl

View Article Online
DOI: 10.1039/D5TA03824C

groups (C=O) at 530.2 ± 0.2 eV and (ii) hydroxyl oxygen (-O-H) species with characteristic binding energy of 531.6 ± 0.2 eV[36]. These comprehensive analyses conclusively demonstrate the development of a high-performance composite system combining MOG and PANI components through a novel in-situ gel-confined polymerization process.

3.2 Electrochemical characterizations

To systematically examines the correlation between PANI content variations and the electrochemical characteristics of MOG/PANI hybrid materials, this study synthesized a series of electrode materials through in situ polymerization, including pristine MOG and PANI-incorporated composites (MOG/PANI-1 to 5) with gradient PANI mass ratios. Figure 5a presents comparative cyclic voltammetry (CV) profiles recorded at 5 mV s^{-1} within a potential window of 0-0.8 V, revealing distinct capacitive behaviors among the six materials. To ensure the rigorous evaluation of electrochemical performance, CV and galvanostatic charge-discharge measurements were conducted on the blank current collector (foam nickel) as a control. As illustrated in Figure S5, the specific capacitance of the current collector is exceedingly low and can be considered negligible when compared to that of the MOG/PANI-x series samples. The cyclic voltammetry curves of all tested samples displayed quasi-rectangular shapes with negligible redox peaks, revealing typical electric double-layer capacitive characteristics. Particularly, the MOG/PANI-3 composite showed significantly expanded CV loop dimensions relative to both pure MOG and other PANI-modified counterparts, demonstrating its enhanced charge storage capacity and

View Article Online
DOI: 10.1039/D5TA03824C

optimal charge/discharge efficiency among the series. The CV profiles of MOG and its polyaniline composites (MOG/PANI-1 to 5) under different scanning speeds are presented in Figures S6a-c and S7a-b. Notably, all composite electrodes maintain their original morphological characteristics in CV curves despite scan rate variation, demonstrating remarkable electrochemical stability and capacitance retention during rapid charge-discharge processes. This consistent behavior across the material series confirms the effective integration of PANI components with the MOG matrix, which synergistically enhances the charge storage kinetics while preserving structural integrity under varying operational conditions. Systematic galvanostatic analysis (1 A g^{-1}) reveals distinct charge storage dynamics through the characteristic voltage-time profiles shown in Figure 5b. The near-ideal linearity and mirror symmetry of charge/discharge branches confirm surface-controlled capacitive processes as the primary charge storage mechanism. Notably, the MOG/PANI-3 hybrid electrode demonstrates the longest charge duration compared to other samples, quantitatively verifying its enhanced specific capacitance, in full agreement with the CV-derived capacitance calculations. The galvanostatic charge-discharge (GCD) profiles of MOG and its PANI-modified composites (MOG/PANI-1 to MOG/PANI-5) were recorded across current densities of 1-20 A g^{-1}, with respective data visualization in Figures S6d-f and S7c-d. Specific capacitance (C_{sp}) values derived from Equation (1) revealed distinct electrochemical performance trends. As illustrated in Figure 5c, the MOG/PANI-3 composite achieved a peak C_{sp} of 423.8 F g^{-1} at 1 A g^{-1}, outperforming existing MOFs-based electrodes (Table S1). Notably, this material maintained 56.6%

View Article Online
DOI: 10.1039/D5TA03824C

capacitance retention (240.0 F g^{-1}) at elevated current density (20 A g^{-1}), demonstrating superior rate capability compared to other tested materials. In contrast, control samples displayed inferior performance: pristine MOG showed a capacitance range of 157.5-20.1 F g^{-1} (12.7% retention), while other composites exhibited intermediate values - MOG/PANI-1 (234.3-120.9 F g^{-1}, 51.6%), MOG/PANI-2 (411.3-187.5 F g^{-1}, 45.6%), MOG/PANI-4 (361.3-157.5 F g^{-1}, 43.6%), and MOG/PANI-5 (317.5-169.9 F g^{-1}, 53.5%). The marked performance gap highlights MOG/PANI-3's exceptional electrochemical stability under high-current operation, as evidenced by its significantly higher retention rate relative to all comparative materials. The experimental results demonstrate that the introduction of PANI remarkably improves the electrochemical performance of MOG matrices, particularly in terms of specific capacitance retention and high-rate charge/discharge characteristics. This enhancement mechanism mainly stems from the precisely controlled PANI incorporation level, which synergistically optimizes two critical parameters: the charge transfer kinetics within the porous framework and the overall electronic conduction pathways of the composite material.

To further investigate the impact of PANI incorporation on the electrochemical impedance characteristics of MOG, EIS curves of composites with varying PANI contents were systematically evaluated (Figures 5f-g). The impedance behavior of supercapacitor electrodes is well-established to comprise three principal elements: (i) equivalent series resistance (R_s); (ii) charge transfer resistance (R_{ct}); and (iii) Warburg impedance (Z_W). Nyquist plot-derived equivalent circuit models are conventionally

View Article Online
DOI: 10.1039/D5TA03824C

utilized to interpret these parameters: the real-axis intercept (Z') corresponds to R_s, the semicircular arc in high-frequency domains reflects R_{ct}, and the low-frequency linear slope correlates with Z_W. Notably, porous electrodes frequently deviate from idealized impedance profiles due to frequency dispersion phenomena arising from structural heterogeneity[37]. To address these complexities, a dual constant phase element (CPE)-integrated circuit was implemented to model the impedance characteristics of MOG-PANI-x electrodes (Figure 5h, inset). This approach accounts for frequency-dependent inhomogeneities in charge distribution and interfacial kinetics. The comprehensive fitting outcomes across all electrode variants were systematically presented in Figure 5h. All MOG/PANI-x electrodes exhibit comparable series resistances (R_s). Specifically, these values are 1.09 Ω for MOG/PANI-1, 0.92 Ω for MOG/PANI-2, 0.77 Ω for MOG/PANI-3, 0.67 Ω for MOG/PANI-4, and 0.63 Ω for MOG/PANI-5. These figures are marginally lower than the resistance of pristine MOG (6.68 Ω), suggesting that incorporating PANI can decrease the equivalent series resistance of MOG component. Additionally, the electrical conductivity of the compressed pellets of the MOG/PANI-x samples was measured using the four-point probe method. It was found that the conductivity of pure MOG is very low (< 10^{-6} S cm^{-1}); an accurate value could not be determined due to exceeding the instrument's detection limit. The measurable conductivities for MOG/PANI-2, MOG/PANI-3, MOG/PANI-4, and MOG/PANI-5 were 1.4×10^{-4}, 3.2×10^{-4}, 8.7×10^{-4}, and 1.1×10^{-3} S cm^{-1}, respectively. This indicates that incorporating PANI effectively enhances the conductivity of MOG. Although the EIS results are not

View Article Online
DOI: 10.1039/D5TA03824C

directly comparable with these values due to the influence of the current collector and conductive additives, both measurements exhibit the same fundamental trend, demonstrating the electrical conductivity enhancement effect of introducing PANI. In the high-frequency part of Nyquist plots, the semicircle relates to the charge-transfer resistance. These were determined to be 5.98 Ω for pristine MOG, 4.87 Ω for MOG/PANI-1, 3.07 Ω for MOG/PANI-2, 1.62 Ω for MOG/PANI-3, 2.06 Ω for MOG/PANI-4, and 3.81 Ω for MOG/PANI-5. This indicates that MOG/PANI-3 demonstrates superior charge-accessibility at the electrode-electrolyte interface compared to other configurations. It is also demonstrated that the electrochemical impedance properties of all MOFs gels have been significantly enhanced following the incorporation of PANI. Furthermore, the slope of the line in the low-frequency region correlates with the ionic diffusion kinetics of the system. The EIS curves show that all PANI-containing samples exhibit slopes greater than 45° in the low-frequency range, indicating that the capacitance arises from the synergistic contribution of pseudocapacitance and electric double-layer capacitance[38]. Moreover, compared to the pristine MOF material, all composite samples display steeper low-frequency slopes after PANI addition, signifying lower Warburg impedance. This is due to the formation of efficient conductive pathways within the composite, facilitating rapid and efficient transport of both electrons and ions, thereby enhancing the ionic diffusion kinetics.

To conduct comprehensive performance evaluations, we employed a multivariate analysis approach using Radar chart visualization (Figure 5i) that simultaneously

View Article Online
DOI: 10.1039/D5TA03824C

assessed four pivotal supercapacitor metrics: (i) gravimetric capacitance (determined at 1 A g^{-1} current density), (ii) current response stability (quantified by capacity retention at 20 A g^{-1}), (iii) interfacial charge-transfer kinetics (expressed as reciprocal charge-transfer resistance $1/R_{ct}$), and (iv) bulk conductivity characteristics (represented by inverse series resistance $1/R_s$). The comparative analysis reveals that unmodified MOG demonstrates worst electrochemical responses across all evaluated parameters. Significantly enhanced multifunctional performance emerges in MOG/PANI-x hybrid architectures following polyaniline integration, with notable improvements observed in both charge transport dynamics and conductive network formation. This synergistic enhancement principally originates from PANI's dual functionality as both structural modifier and high-performance conductive medium, which effectively optimizes electron migration pathways and reduces interfacial impedance in the composite system. As illustrated in Figure S8, PANI chains can bridge the isolated MOG skeletons, forming electron pathways between the external circuit and MOG surfaces. This integration induces a synergistic effect: the in-situ generated PANI can significantly boost MOG conductivity and intensify interfacial Faradaic reactions. Consequently, the resulting hybrid electrode architecture successfully combines the advantages of the inherent porosity derived from the ordered metal-organic frameworks of MOF and the efficient charge transport network established by PANI. As a result, there is a notable improvement in specific capacitance and rate capability. Moreover, it can be intuitively observed that with the increase in PANI content, the equivalent series resistance of the composite gel

View Article Online
DOI: 10.1039/D5TA03824C

gradually decreases. Nevertheless, the charge transfer resistance does not exhibit the same tendency. When the PANI content is relatively low, such as in samples MOG/PANI-1, MOG/PANI-2 and MOG/PANI-3, the charge transfer resistance gradually reduces as the PANI content increases. With the continuous increase in PANI content, the charge transfer resistance of MOG/PANI-4 and MOG/PANI-5 starts to rebound. Considering the results of morphological analysis, this might be attributed to the excessive PANI causing local agglomeration and significant non-uniformity in the composite structure, thereby reducing the effective charge transfer paths. Consequently, the composites with high PANI content possess worse charge transfer performance compared to those with low PANI content. Influenced by this, the change of specific capacitance of the composites also presents a similar pattern. Additionally, the theoretical specific capacitance of PANI is lower than that of MOFs-based electrode materials. The high content of PANI further dilutes the specific capacity contribution of MOG, resulting in the maximum specific capacitance of the composites occurring at MOG/PANI-3. The rate performance demonstrates a more complex changing trend, as it is comprehensively affected by various factors, including the conductivity of the material, charge transfer characteristics, structural uniformity, and the rate performance of the original PANI and MOG themselves. Under the combined influence of these factors, the rate performance of the composites presents four turning points. MOG/PANI-3 exhibits relatively outstanding performance in all aspects. Therefore, under the combined effect, its rate performance is also the best. In summary, incorporating PANI substantially improves the energy

View Article Online
DOI: 10.1039/D5TA03824C

storage properties of the MOG material. Among all samples, MOG/PANI-3 exhibits the optimal composite structure and the most favorable composite ratio.

3. 3 Electrochemical studies of the QSLHC device

In order to evaluate practical performance, a quasi-solid-state lithium-ion hybrid capacitor (QSLHC) incorporating PVA-Li_2SO_4 gel electrolyte was constructed. The device configuration utilized MOG/PANI-3 composite as cathode material paired with commercially available activated carbon (AC) as anode, as illustrated in Figure 6a. Figure S9a demonstrates CV curves of AC recorded between -1.0 and 0 V potential window across scan rates spanning 5-100 mV s^{-1}, indicative of capacitive behavior. Complementary GCD curves in Figure S9b display characteristic linear voltage-time responses with symmetrical triangular shapes, maintaining consistency with CV observations. The electrochemical measurements revealed that the AC electrode exhibited a specific capacitance of 228.1 F g^{-1} when subjected to a current density of 1 A g^{-1}, as calculated through equation (1). To optimize the device's electrochemical properties, the optimal mass ratio between MOG/PANI-3 and AC was determined as approximately 0.65. This ratio was calculated based on equation (2). The QSLHC system demonstrated ideal capacitive behavior with symmetrical CV curves within the 0-1.8 V range, indicating effective charge storage behavior. Subsequent electrochemical characterization involved recording CV profiles across varying scan rates (5-100 mV s^{-1}) under identical voltage conditions (Figure 6b), revealing stable performance across different charge/discharge kinetics. No significant distortion is evident in the curve shapes, demonstrating a satisfactory rate

View Article Online
DOI: 10.1039/D5TA03824C

capability. Additionally, the GCD curves presented in Figure 6c maintain good symmetry under different current densities, which reflects acceptable electrochemical reversibility and high Coulombic efficiency. Figure 6d illustrates the relationship between calculated specific capacitance (C_{sp}) and current density for the QSLHC device. The maximum C_{sp} of 91.7 F g^{-1} is obtained at 1 A g^{-1}, while a significant reduction to 23.4 F g^{-1} (25.5% retention) occurs when current density increases to 20 A g^{-1}. In addition, the device's energy density (E) and power density (P) were obtained using formulas $E = C_{sp}(\Delta V)^2/7.2$ and $P = 3600E/\Delta t$, respectively. Given that the mass fraction of the active material in the entire device (comprising the packaging shell, dual-electrode current collector foam nickel, positive and negative electrode active materials, PVA gel electrolyte, conductive agent, binder, and tab) accounts for 1.2 wt%, the device-level energy density (E_{device}) and power density (P_{device}) are determined based on the formulas $E_{device} = 1.2\% \times E$ and $P_{device} = 1.2\% \times P$, which serve as key references for evaluating the overall device performance. The Ragone plot in Figure 6e highlights the QSLHC's energy-storage performance, where the MOG/PANI-3//AC configuration delivers a peak energy density of 41.3 Wh kg^{-1} at 900 W kg^{-1} (E_{device} = 0.496 Wh kg^{-1}; P_{device} =10.8 W kg^{-1}). Notably, even under extreme conditions of 18.0 kW kg^{-1} power density, the system sustains 10.5 Wh kg^{-1} energy density (E_{device} = 0.126 Wh kg^{-1}; P_{device} =216 W kg^{-1}). These results surpass those of MOFs-based ASC (Asymmetric Supercapacitor) and SSC (Symmetrical Supercapacitor) devices, such as HKUST-1/PANI//rGO ASC (6.22 W h kg^{-1}, 374.52 W kg^{-1})[39], CoMn-MOF//graphene ASC (17.9 W h kg^{-1}, 785.7 W kg^{-1})[40],

View Article Online
DOI: 10.1039/D5TA03824C

rGO/Ppy/Zn-MOF SSC (19.7 W h kg^{-1}, 1792 W kg^{-1})[41], Ni-MOF@PPy//AC ASC (38.5 W h kg^{-1}, 400 W kg^{-1})[42], Cu-MOF//Cu-MOF SSC (18.2 W h kg^{-1}, 825 W kg^{-1})[43], AC//MOF/PANI ASC (23.2 W h kg^{-1}, 1600 W kg^{-1})[44], ZZCMP-10//AC ASC (26 W h kg^{-1}, 725 W kg^{-1})[45], Cd-MOF//AC ASC (11.25 W h kg^{-1}, 500 W kg^{-1})[46], Ni-MOF@NiS_2//AC ASC (23.5 W h kg^{-1}, 1400 W kg^{-1})[47], and Cu-BGPD//rGO ASC (15.25 W h kg^{-1}, 850 W kg^{-1})[48], etc. Furthermore, the cyclic durability of the electrochemical system was systematically evaluated through extended charge-discharge testing. As evidenced by the data in Figure 6f, the developed QSLHC architecture demonstrates acceptable capacity retention, preserving 87.3% of its initial capacitance through 4000 continuous GCD tests when examined at 5 A g^{-1} current density. This performance is credited to the exceptional incorporation architecture of MOG/PANI-3. The precise layout of the assembled MOG/PANI-3//AC device is illustrated in the inset of Figure 6f. Following a complete charging cycle, the QSLHC device demonstrates operational efficacy in driving timing circuit indicator, thereby validating its feasibility for real-world implementation. This experimental evidence substantiates that MOG/PANI composite electrodes exhibit superior electrochemical characteristics, enabling them as innovative candidates for advanced energy storage systems design.

4. Conclusions

In conclusion, a new in-situ gel-confined polymerization approach has been introduced for the formation of the MOFs/PANI composite gel structure. By progressively adjusting the amount of added PANI, it was observed that the

View Article Online
DOI: 10.1039/D5TA03824C

compositions exhibit varying morphologies and electrochemical characteristics. The MOG/PANI-3 sample demonstrates uniform distribution and strong interactions between the MOG matrix and the PANI component. The MOG/PANI-3 composite demonstrates superior electrochemical performance as an electrode material, exhibiting a high specific capacitance of 423.8 F g^{-1} under 1 A g^{-1}. This optimized configuration simultaneously maintains an operational potential window of 0.8 V. Notably, overdosage of PANI during synthesis could induce heterogeneous aggregation phenomena, which detrimentally affects the electrode's charge transfer characteristics by disrupting homogeneous impedance distribution. A proof-of-concept quasi-solid-state lithium-ion hybrid capacitor was engineered by pairing the MOG/PANI-3 cathode with activated carbon anode in PVA-Li_2SO_4 gel polymer electrolyte matrix. The resultant device delivers competitive energy storage characteristics, achieving 41.3 W h kg^{-1} energy density at 900 W kg^{-1} power output. Moreover, the system shows acceptable electrochemical durability with 87.3% capacitance retention after 4000 galvanostatic cycles at 5 A g^{-1}, demonstrating promising practical applicability. The findings propose a novel methodology for engineering MOF-based composite architectures. This study highlights new opportunities in designing complicated multiphase hybrid materials with enhanced capabilities for next-generation energy storage solutions.

Acknowledgements

This work was financially supported by the National Natural Science Foundation of China (NSFC Grants 52302313) and Postgraduate Research & Practice Innovation

View Article Online
DOI: 10.1039/D5TA03824C

Program of Yancheng Institute of Technology (KYCX25_XY006).

Conflict of Interests

The authors certify that they have NO affiliations with or involvement in any organization or entity with any financial or non-financial interest in the subject matter or materials discussed in this manuscript.

Data Availability Statement

The data that support the findings of this study are available in the supplementary material of this article. Any other information should be requested to the corresponding authors.

References

[1] K. Ge, H. Shao, Z. Lin, P.-L. Taberna, P. Simon, Advanced characterization of confined electrochemical interfaces in electrochemical capacitors, *Nat. Nanotechnol.*, **2025**, *20*, 196-208. https://doi.org/10.1038/s41565-024-01821-z.

[2] Z. Wang, T. Wu, L. Zeng, J. Peng, X. Tan, D. Yu, M. Gao, G. Feng, Machine Learning Relationships Between Nanoporous Structures and Electrochemical Performance in MOF Supercapacitors, *Adv. Mater.*, **2025**, *37*, 2500943. https://doi.org/10.1002/adma.202500943.

[3] C. Cheng, Y. Yan, M. Jia, Y. Liu, L. Hou, C. Yuan, Insights into Formation and Li-Storage Mechanisms of Hierarchical Accordion-Shape Orthorhombic $CuNb_2O_6$ toward Lithium-Ion Capacitors as an Anode-Active Material, *Energy Environ. Mater.*, **2024**, *7*, e12583. https://doi.org/10.1002/eem2.12583.

[4] J. Yin, W. Zhang, N.A. Alhebshi, N. Salah, H.N. Alshareef, Synthesis Strategies of Porous Carbon for Supercapacitor Applications, *Small Methods*, **2020**, *4*, 1900853. https://doi.org/10.1002/smtd.201900853.

[5] P. Ghasemiahangarani, G. Farhan, D. del Mundo, T. Schoetz, Charge Storage Mechanisms in Batteries and Capacitors: A Perspective of the Electrochemical Interface, *Adv. Energy Mater.*, **2025**, *15*, 2404704. https://doi.org/10.1002/aenm.202404704.

[6] C. Cheng, D. Wu, T. Gong, Y. Yan, Y. Liu, W. Ji, L. Hou, C. Yuan, Internal and External Cultivation Design of Zero-Strain Columbite-Structured MNb_2O_6 toward Lithium-Ion Capacitors as Competitive Anodes, *Adv. Energy Mater.*, **2023**, *13*, 2302107. https://doi.org/10.1002/aenm.202302107.

[7] N. Choudhary, C. Li, J. Moore, N. Nagaiah, L. Zhai, Y. Jung, J. Thomas, Asymmetric Supercapacitor Electrodes and Devices, *Adv. Mater.*, **2017**, *29*, 1605336. https://doi.org/10.1002/adma.201605336.

[8] J. He, L. Cao, J. Cui, G. Fu, R. Jiang, X. Xu, C. Guan, Flexible Energy Storage Devices to Power the Future, *Adv. Mater.*, **2024**, *36*, 2306090. https://doi.org/10.1002/adma.202306090.

[9] B. He, Q. Zhang, Z. Pan, L. Li, C. Li, Y. Ling, Z. Wang, M. Chen, Z. Wang, Y. Yao, Q. Li, L. Sun, J. Wang, L. Wei, Freestanding Metal-Organic Frameworks and Their Derivatives: An Emerging Platform for Electrochemical Energy Storage and Conversion, *Chem. Rev.*, **2022**, *122*, 10087-10125. https://doi.org/10.1021/acs.chemrev.1c00978.

[10] W. Wang, D. Chen, F. Li, X. Xiao, Q. Xu, Metal-organic-framework-based materials as platforms for energy applications, *Chem*, **2024**, *10*, 86-133. https://doi.org/10.1016/j.chempr.2023.09.009.

[11] H. Wang, Q. Yang, N. Zheng, X. Zhai, T. Xu, Z. Sun, L. Wu, M. Zhou, Roadmap of amorphous metal-organic framework for electrochemical energy conversion and storage, *Nano Res.*, **2023**, *16*, 4107-4118.

View Article Online
DOI: 10.1039/D5TA03824C

https://doi.org/10.1007/s12274-022-5114-8.

[12] K.O. Otun, A. Mukhtar, S.A. Nafiu, I.T. Bello, J. Abdulsalam, Incorporation of redox-activity into metal-organic frameworks for enhanced supercapacitors: A review, *J. Energy Storage*, **2024**, *84*, 110673. https://doi.org/10.1016/j.est.2024.110673.

[13] P. Dubey, V. Shrivastav, S. Sundriyal, P.H. Maheshwari, Sustainable Nanoporous Metal-Organic Framework/Conducting Polymer Composites for Supercapacitor Applications, *ACS Appl. Nano Mater.*, **2024**, *7*, 18554-18565. https://doi.org/10.1021/acsanm.4c01697.

[14] S. Yang, V.V. Karve, A. Justin, I. Kochetygov, J. Espín, M. Asgari, O. Trukhina, D.T. Sun, L. Peng, W.L. Queen, Enhancing MOF performance through the introduction of polymer guests, *Coord. Chem. Rev.*, **2021**, *427*, 213525. https://doi.org/10.1016/j.ccr.2020.213525.

[15] H.N. Heme, M.S.N. Alif, S.M.S.M. Rahat, S.B. Shuchi, Recent progress in polyaniline composites for high capacity energy storage: A review, *J. Energy Storage*, **2021**, *42*, 103018. https://doi.org/10.1016/j.est.2021.103018.

[16] V.J. Vipu Vinayak, K. Deshmukh, V.R.K. Murthy, S.K.K. Pasha, Conducting polymer based nanocomposites for supercapacitor applications: A review of recent advances, challenges and future prospects, *J. Energy Storage*, **2024**, *100*, 113551. https://doi.org/10.1016/j.est.2024.113551.

[17] A.P.M. Udayan, O. Sadak, S. Gunasekaran, Metal-Organic Framework/Polyaniline Nanocomposites for Lightweight Energy Storage, *ACS Appl. Energy Mater.*, **2020**, *3*, 12368-12377. https://doi.org/10.1021/acsaem.0c02376.

[18] L. Wang, X. Feng, L. Ren, Q. Piao, J. Zhong, Y. Wang, H. Li, Y. Chen, B. Wang, Flexible Solid-State Supercapacitor Based on a Metal-Organic Framework

Interwoven by Electrochemically-Deposited PANI, *J. Am. Chem. Soc.*, **2015**, *137*, 4920-4923. https://doi.org/10.1021/jacs.5b01613.

[19] C. Zhu, Y. He, Y. Liu, N. Kazantseva, P. Saha, Q. Cheng, ZnO@MOF@PANI core-shell nanoarrays on carbon cloth for high-performance supercapacitor electrodes, *J. Energy Chem.*, **2019**, *35*, 124-131. https://doi.org/10.1016/j.jechem.2018.11.006.

[20] S. Guo, Y. Zhu, Y. Yan, Y. Min, J. Fan, Q. Xu, H. Yun, (Metal-Organic Framework)-Polyaniline sandwich structure composites as novel hybrid electrode materials for high-performance supercapacitor, *J. Power Sources*, **2016**, *316*, 176-182. https://doi.org/10.1016/j.jpowsour.2016.03.040.

[21] S. Maity, S. Bera, A. Kapuria, A. Debnath, S. Das, S.K. Saha, MXene derived metal organic framework@PANI heterostructure as a hybrid supercapacitor, *Mater. Today Chem.*, **2025**, *45*, 102690. https://doi.org/10.1016/j.mtchem.2025.102690.

[22] M. Kim, J.F. Cahill, H. Fei, K.A. Prather, S.M. Cohen, Postsynthetic Ligand and Cation Exchange in Robust Metal-Organic Frameworks, *J. Am. Chem. Soc.*, **2012**, *134*, 18082-18088. https://doi.org/10.1021/ja3079219.

[23] S. Xiang, L. Li, J. Zhang, X. Tan, H. Cui, J. Shi, Y. Hu, L. Chen, C.-Y. Su, S.L. James, Porous organic–inorganic hybrid aerogels based on Cr^{3+}/Fe^{3+} and rigid bridging carboxylates, *J. Mater. Chem.*, **2012**, *22*, 1862-1867. https://doi.org/10.1039/C1JM14618A.

[24] Y. Wang, Y. Zhang, R. Shao, Q. Guo, FeSe and Fe_3Se_4 encapsulated in mesoporous carbon for flexible solid-state supercapacitor, *Chem. Eng. J.*, **2022**, *442*, 136362. https://doi.org/10.1016/j.cej.2022.136362.

[25] Y. Wang, H. Tang, Q. Xie, J. Liu, S. Sun, M. Zhou, Y. Zhang, pH-Regulated host-guest architecture in molybdenum Dioxide/Carbon sphere composites for flexible solid-state supercapacitors, *Chem. Eng. J.*, **2024**, *481*, 148558.

View Article Online
DOI: 10.1039/D5TA03824C

https://doi.org/10.1016/j.cej.2024.148558.

[26] J. Hou, A.F. Sapnik, T.D. Bennett, Metal-organic framework gels and monoliths, *Chem. Sci.*, **2020**, *11*, 310-323. https://doi.org/10.1039/C9SC04961D.

[27] H. Wang, B.-H. Chen, D.-J. Liu, Metal–Organic Frameworks and Metal-Organic Gels for Oxygen Electrocatalysis: Structural and Compositional Considerations, *Adv. Mater.*, **2021**, *33*, 2008023. https://doi.org/10.1002/adma.202008023.

[28] G. Férey, C. Serre, C. Mellot-Draznieks, F. Millange, S. Surblé, J. Dutour, I. Margiolaki, A Hybrid Solid with Giant Pores Prepared by a Combination of Targeted Chemistry, Simulation, and Powder Diffraction, *Angew. Chem. Int. Ed.*, **2004**, *43*, 6296-6301. https://doi.org/10.1002/anie.200460592.

[29] Y. Wang, J. Liu, H. Cao, J. Ding, N. Wang, C. He, Y. Zhang, Facile synthesis of porous high-entropy perovskite nanoparticles through MOF gel method for solid-state supercapacitor application, *Chem. Eng. J.*, **2025**, *509*, 161246. https://doi.org/10.1016/j.cej.2025.161246.

[30] R.R. Gopi, T. Ebenezer, H.J. Prabu, I. Johnson, W. Galeb, M.D. Raja, S.J. Sundaram, J.S.K. Arockiasamy, A.F. Sahayaraj, Synthesis and investigation of charge storage characteristics in Ni-MOF/PANI composite as an active electrode material for supercapacitor, *Electrochim. Acta*, **2024**, *507*, 145130. https://doi.org/10.1016/j.electacta.2024.145130.

[31] E. Gkaniatsou, R. Ricoux, K. Kariyawasam, I. Stenger, B. Fan, N. Ayoub, S. Salas, G. Patriarche, C. Serre, J.-P. Mahy, N. Steunou, C. Sicard, Encapsulation of Microperoxidase-8 in MIL-101(Cr)-X Nanoparticles: Influence of Metal-Organic Framework Functionalization on Enzymatic Immobilization and Catalytic Activity, *ACS Appl. Nano Mater.*, **2020**, *3*, 3233-3243. https://doi.org/10.1021/acsanm.9b02464.

[32] C. Constantinescu, N. Scarisoreanu, A. Moldovan, M. Dinescu, C. Vasiliu, Thin films of polyaniline deposited by MAPLE technique, *Appl. Surf. Sci.*, **2007**, *253*, 7711-7714. https://doi.org/10.1016/j.apsusc.2007.02.057.

[33] J. Chi, S. Gu, R. Shi, R. Zhao, X. Liu, Q. Zhang, Q. Lv, Z. Xiao, L. Wang, Extending PANI molecular chains into pores of hierarchical MIL-101 as flexible electrodes for supercapacitor applications, *Chem. Eng. J.*, **2025**, *510*, 161764. https://doi.org/10.1016/j.cej.2025.161764.

[34] Y.D. Zhang, Q. Xie, R. Shao, J.F. Ding, J.L. Liu, W. Xu, Y. Wang, Green synthesis of MOF/CNT gels via in-situ physical mixing strategy toward quasi-solid-state Li-ion hybrid capacitor, *Journal of Energy Storage*, **2024**, *86*, 111156. https://doi.org/10.1016/j.est.2024.111156.

[35] D. Xia, Y. Liu, X. Cheng, P. Gu, Q. Chen, Z. Zhang, Temperature-tuned fish-scale biochar with two-dimensional homogeneous porous structure: A promising uranium extractant, *Appl. Surf. Sci.*, **2022**, *591*, 153136. https://doi.org/10.1016/j.apsusc.2022.153136.

[36] M. Yang, X. Liu, B. Wu, W. Chen, X. Song, J. Liu, Z. Nan, M. Zhang, L. Zhang, Non-uniform polarization boosted electromagnetic wave absorption with high efficiency and a broad frequency range, *Mater. Today Chem.*, **2024**, *39*, 102180. https://doi.org/10.1016/j.mtchem.2024.102180.

[37] D. Saha, Y. Li, Z. Bi, J. Chen, J.K. Keum, D.K. Hensley, H.A. Grappe, H.M. Meyer, III, S. Dai, M.P. Paranthaman, A.K. Naskar, Studies on Supercapacitor Electrode Material from Activated Lignin-Derived Mesoporous Carbon, *Langmuir*, **2014**, *30*, 900-910. https://doi.org/10.1021/la404112m.

[38] S. Liu, M. Jia, F. Chu, H. Jiang, J. Jia, J. Sun, Y. Liu, L. Hou, C. Yuan, Commercializable Fluorine-Doped Porous Carbon Toward Advanced 4.5 V-Class

Lithium-Ion Capacitors, *Energy Environ. Mater.*, **2025**, *8*, e70002. https://doi.org/10.1002/eem2.70002.

[39] E.A. Jafari, M. Moradi, S. Borhani, H. Bigdeli, S. Hajati, Fabrication of hybrid supercapacitor based on rod-like HKUST-1@polyaniline as cathode and reduced graphene oxide as anode, *Physica E*, **2018**, *99*, 16-23. https://doi.org/10.1016/j.physe.2018.01.007.

[40] T.-M. Cheng, C.-H. Hsieh, L.-D. Shang, Y.-M. Fan, S. Yougbaré, L.-Y. Lin, Y.-F. Wu, Effects of metal ratios and post treatments on energy storage ability of cobalt manganese metal organic frameworks, *J. Energy Storage*, **2023**, *68*, 107730. https://doi.org/10.1016/j.est.2023.107730.

[41] N. Saxena, M.P. Bondarde, K.D. Lokhande, M.A. Bhakare, P.S. Dhumal, S. Some, One-pot synthesis of rGO/Ppy/Zn-MOF, ternary composite for High-Performance supercapacitor application, *Chem. Phys. Lett.*, **2024**, *856*, 141605. https://doi.org/10.1016/j.cplett.2024.141605.

[42] Z. Qin, Y. Xu, L. Liu, M. Liu, H. Zhou, L. Xiao, Y. Cao, C. Chen, Ni-MOF composite polypyrrole applied to supercapacitor energy storage, *RSC Adv.*, **2022**, *12*, 29177-29186. https://doi.org/10.1039/D2RA04939B.

[43] P. Dubey, V. Shrivastav, P.H. Maheshwari, M. Hołdyński, A. Krawczyńska, S. Sundriyal, Comparative study of different metal-organic framework electrodes synthesized using waste PET bottles for supercapacitor applications, *J. Energy Storage*, **2023**, *68*, 107828. https://doi.org/10.1016/j.est.2023.107828.

[44] M.Z. Iqbal, M.M. Faisal, S.R. Ali, S. Farid, A.M. Afzal, Co-MOF/polyaniline-based electrode material for high performance supercapattery devices, *Electrochim. Acta*, **2020**, *346*, 136039. https://doi.org/10.1016/j.electacta.2020.136039.

[45] D. Qin, B. Zhou, Z. Li, C. Yang, Construction of controllable multicomponent

ZnO-ZnCo/MOF-PANI composites for supercapacitor applications, *J. Mol. Struct.*, **2024**, *1309*, 138140. https://doi.org/10.1016/j.molstruc.2024.138140.

[46] R. Deka, R. Rajak, V. Kumar, S.M. Mobin, Effect of Electrolytic Cations on a 3D Cd-MOF for Supercapacitive Electrodes, *Inorg. Chem.*, **2023**, *62*, 3084-3094. https://doi.org/10.1021/acs.inorgchem.2c03879.

[47] J. Zhang, Y. Li, M. Han, Q. Xia, Q. Chen, M. Chen, Constructing ultra-thin Ni-MOF@NiS_2 nanosheets arrays derived from metal organic frameworks for advanced all-solid-state asymmetric supercapacitor, *Mater. Res. Bull.*, **2021**, *137*, 111186. https://doi.org/10.1016/j.materresbull.2020.111186.

[48] H. Rong, G. Gao, X. Liu, X. Chen, Q. Jiang, X. Song, D. Shen, W. Liu, Q. Liu, Asymmetric Supercapacitor Based on a 1D Cu-Coordination Polymer with High Cycle Stability, *Cryst. Growth Des.*, **2023**, *23*, 5437-5445. https://doi.org/10.1021/acs.cgd.2c01305.

View Article Online
DOI: 10.1039/D5TA03824C

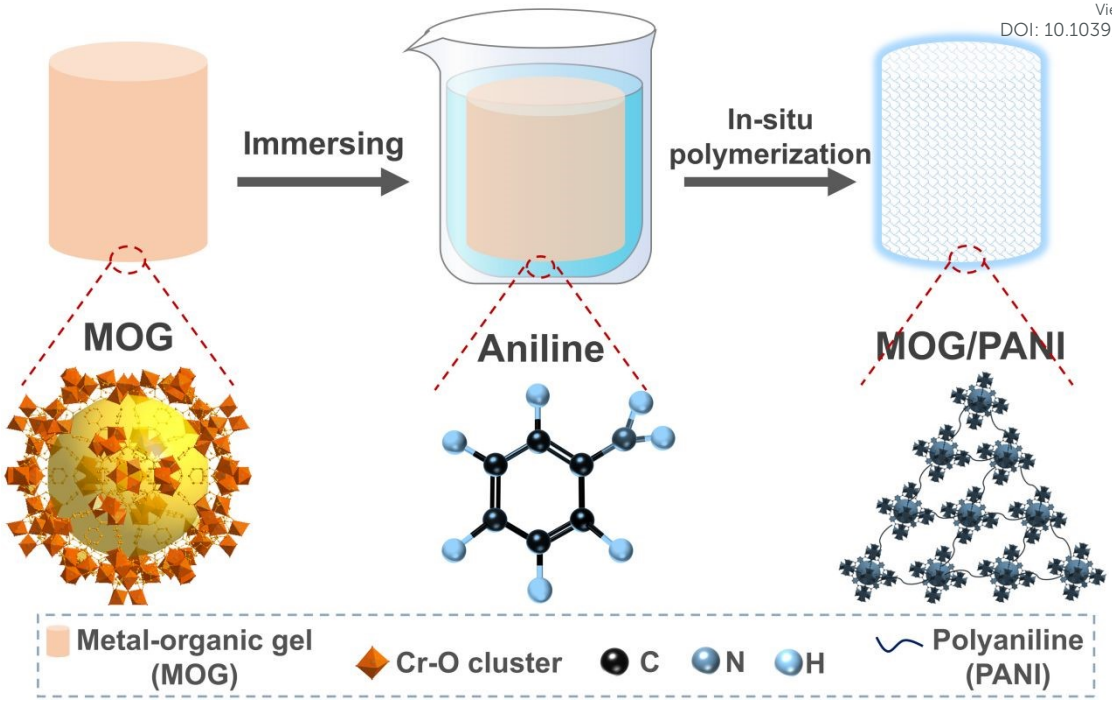

Figure 1 Schematic illustration of the fabrication process of MOG/PANI composites.

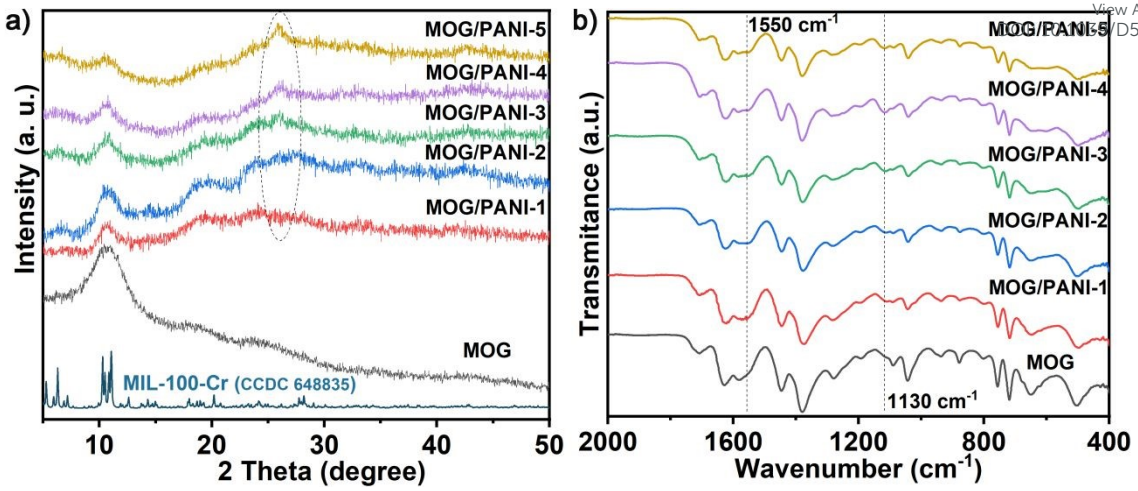

Figure 2 (a) XRD patterns and (b) FTIR spectra of MOG/PANI-x composites.

View Article Online
DOI: 10.1039/D5TA03824C

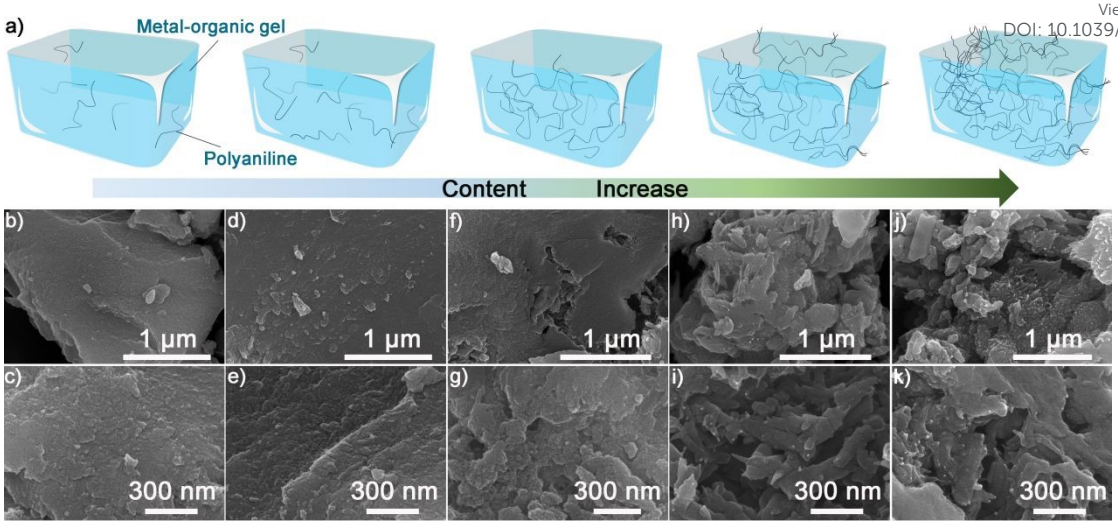

Figure 3 (a) Schematic representation of morphology transition of MOG/PANI-x composites with the increase of PANI content; and the corresponding FESEM images at different scales of (b), (c) MOG/PANI-1; (d), (e) MOG/PANI-2; (f), (g) MOG/PANI-3; (h), (i) MOG/PANI-4; (j), (k) MOG/PANI-5.

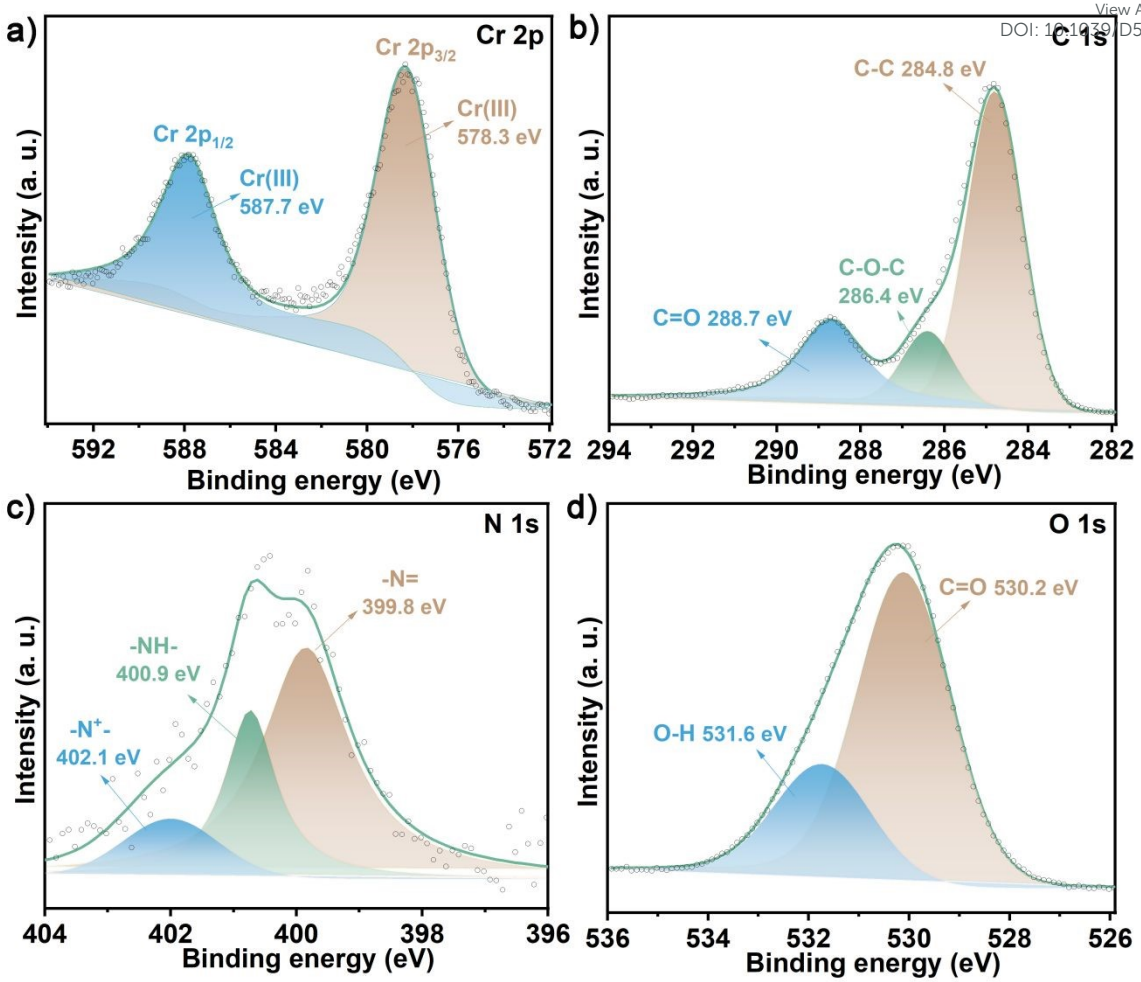

Figure 4 High resolution XPS spectra of MOG/PANI-3: (a) Cr 2p, (b) C 1s, (c) N 1s, (d) O 1s.

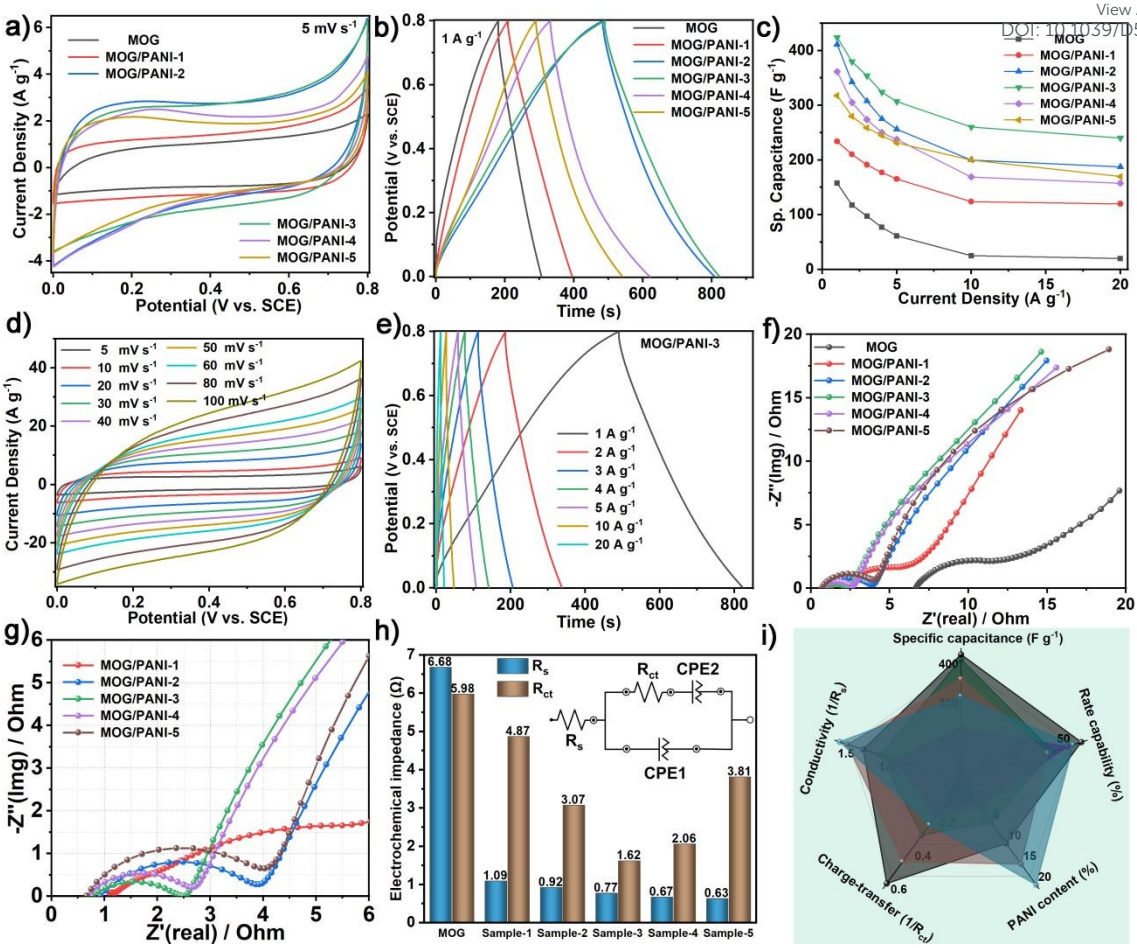

Figure 5 Electrochemical performance of MOG/PANI-x composites in the three-electrode cell: (a) comparative CV curves at 5 mV s^{-1}; (b) comparative GCD curves at 1 A g^{-1}; (c) calculated Q_{sp} values at different current density; (d) CV curves of MOG/PANI-3 at different scan rates; (e) GCD curves of MOG/PANI-3 at different current densities; (f) comparative Nyquist plots; (g) the magnified views of Nyquist plots; (h) electrode impedance fitting results and equivalent circuit diagram (inset); (i) comparison Radar chart.

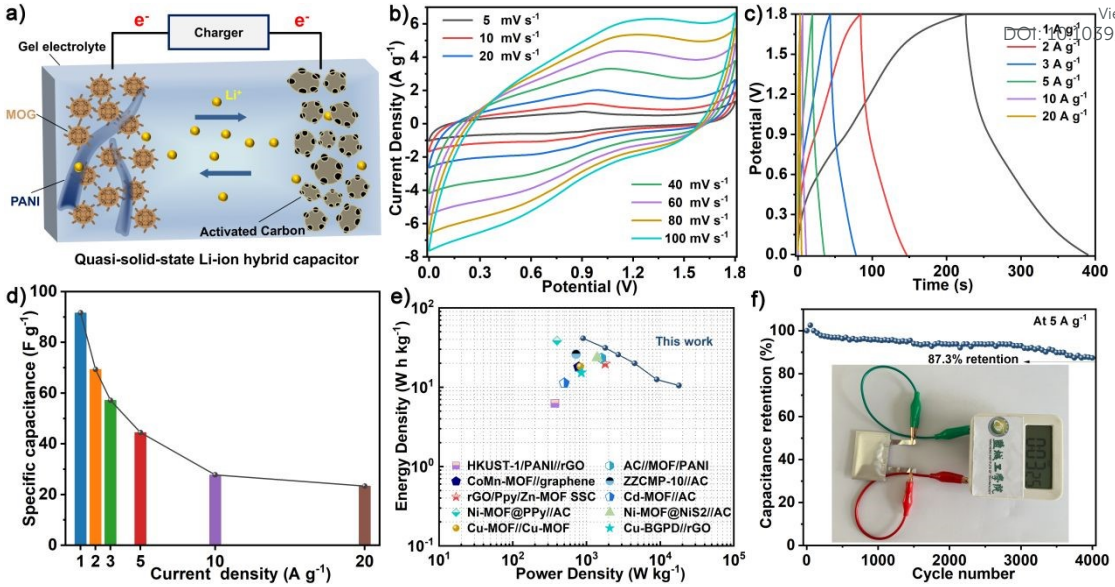

Figure 6 Electrochemical characterization of the as-assembled MOG/PANI-3//AC QSLHC device: (a) schematic of the device configuration; (b) CV curves with a voltage window of 1.8 V at different scan rates; (c) GCD curves at different current densities; (d) Specific capacitance of QSLHC vs current density; (e) Ragone plot related to energy and power densities; (f) cycling performance over 4000 cycles at 5 A g^{-1}, inset: Photograph of the QSLHC devices, driving a timing circuit indicator after charged.

View Article Online
DOI: 10.1039/D5TA03824C

Data Availability Statement

The data that support the findings of this study are available in the supplementary material of this article. Any other information should be requested to the corresponding authors.